IX CONGRESSO BRASILEIRO DE
ENGENHARIA E CIÊNCIAS TÉRMICAS
9th BRAZILIAN CONGRESS OF THERMAL
ENGINEERING AND SCIENCES

Paper CIT02-0341

ON TURBULENCE MODELS FOR 3-D AEROSPACE APPLICATIONS

Enda Dimitri Vieira Bigarelli
Instituto Tecnológico de Aeronáutica, Centro Técnico Aeroespacial, São José dos Campos, SP, BRAZIL – 12228-900
enda.bigarelli@ig.com.br

João Luiz F. Azevedo
Instituto de Aeronáutica e Espaço, Centro Técnico Aeroespacial, São José dos Campos, SP, BRAZIL – 12228-904
azevedo@iae.cta.br

Abstract. *Turbulent flow simulations are presented in this paper. A 3-D finite difference numerical code, written for general, curvilinear, body-conforming coordinate systems, is used. Simulations of turbulent flows over a flat plate are compared to theoretical results in order to assess the correctness of the implementation of the formulation. Transonic turbulent flows are then simulated about the Brazilian Satellite Launch Vehicle (VLS) configuration, currently under development at IAE. Two eddy viscosity turbulence models are chosen for this numerical method, considering single- and two-equation closures. These two models were natively developed for aerospace applications. In general, good results within engineering error margins are obtained with the method presented here.*

Keywords: *CFD, Turbulent flow, Aerospace configuration.*

1. Introduction

Launch vehicles are typically designed to fly at very low angles of attack. Nevertheless, even at such flight condition, the lateral loads that arise in these vehicles are quite strong and they must be accurately determined. Therefore, during the design process, one is required to determine the aerodynamics of these vehicles at angle of attack because this will provide the loads required for the structural design of the vehicle as well as the flight dynamics stability characteristics necessary for the control system design. Earlier works (Zdravistch and Azevedo, 1990; Azevedo et al., 1991) has presented axisymmetric viscous simulations for flows over the VLS with very good representation of the aerodynamics. Moreover, three-dimensional inviscid computations over the VLS at low angles of attack with good agreement with experimental data were also performed (Azevedo et al., 1996). This earlier work, however, considered fairly simple 3-D geometries and mesh refinement was less than adequate due to computational resource limitations.

Further development in the computational resources in the country made possible the simulation of more realistic flows and, thus, axisymmetric turbulent flows and 3-D laminar viscous flows simulations could be performed with adequate mesh refinement. Furthermore, axisymmetric meshes could be made refined enough to capture the dependency of the formulation with the Reynolds number, as shown by Azevedo and Buonomo, 1999. The results presented in that work showed the influence of the turbulence modelling in the flow configuration. Bigarelli et al., 1999, have shown 3-D results over general launch vehicle configurations. The calculations emphasized that a laminar viscous formulation could not correctly capture some of the flow phenomena that might occur in the simulations of interest at IAE. Obviously, this is what one should expect since the Reynolds numbers of interest are of the order of $Re = 10^7$. Clearly, phenomena such as flow separation due to adverse pressure gradients and shock wave-boundary layer interactions are poorly represented by a laminar formulation at such high Reynolds numbers. Nevertheless, these phehomena play an important role in the flows over launch vehicles and, therefore, should be adequately simulated.

The present work is aimed at addressing the implementation and validation of turbulent closures for the computational tool under development at IAE. Hence, numerical results of the subsonic turbulent flow over a flat plate are compared to known data in the literature in order to assess the correctness of the newly turbulent formulation added to the code. Furthermore, the computational code is used to simulate 3-D transonic flows about the first Brazilian Satellite Launch Vehicle (VLS). This vehicle is a four-stage satellite launcher built with four booster attached to a main body. Since experimental data is available for this configuration, the numerical results are compared to them such that the code effectiveness in the solution of realistic aerospace configuration flows can be assessed. In the present work, computations were performed considering only the vehicle central body. The solver used is a 3-D finite-difference code written for general, body-conforming, curvilinear coordinate systems and it solves the thin-layer approximation of the compressible Reynolds-averaged Navier-Stokes equations.

2. Theoretical Formulation

The numerical code used solves the thin-layer approximation of the 3-D, compressible, turbulent, Reynolds-averaged Navier-Stokes equations. The equations can be written in strong conservation-law form for general, body-conforming, curvilinear coordinates (Pulliam and Steger, 1980) as

$$\frac{\partial \overline{Q}}{\partial \tau} + \frac{\partial \overline{E}}{\partial \xi} + \frac{\partial \overline{F}}{\partial \eta} + \frac{\partial \overline{G}}{\partial \zeta} = \frac{\partial \overline{E}_v}{\partial \xi} + \frac{\partial \overline{F}_v}{\partial \eta} + \frac{\partial \overline{G}_v}{\partial \zeta} \ , \tag{1}$$

where the vector of conserved quantities, $\overline{Q}$, is defined as

$$\overline{Q} = J^{-1} \left[\begin{array}{cccccc} \rho & \rho u & \rho v & \rho w & e \end{array} \right]^{\mathrm{T}} \ . \tag{2}$$

The inviscid flux vectors, $\overline{E}$, $\overline{F}$ and $\overline{G}$, can be written as

$$\overline{E} = J^{-1} \left\{ \begin{array}{c} \rho U \\ \rho u U + p \xi_x \\ \rho v U + p \xi_y \\ \rho w U + p \xi_z \\ (e+p)U - p \xi_t \end{array} \right\} \ , \quad \overline{F} = J^{-1} \left\{ \begin{array}{c} \rho V \\ \rho u V + p \eta_x \\ \rho v V + p \eta_y \\ \rho w V + p \eta_z \\ (e+p)V - p \eta_t \end{array} \right\} \ , \quad \overline{G} = J^{-1} \left\{ \begin{array}{c} \rho W \\ \rho u W + p \zeta_x \\ \rho v W + p \zeta_y \\ \rho w W + p \zeta_z \\ (e+p)W - p \zeta_t \end{array} \right\} \ , \tag{3}$$

and the viscous flux vectors, $\overline{E}_v$, $\overline{F}_v$ and $\overline{G}_v$ can be defined as

$$\begin{aligned}
\overline{E}_v &= \frac{J^{-1}}{Re} \left\{ \begin{array}{c} 0 \\ \mu \left(\xi_x^2 + \xi_y^2 + \xi_z^2\right) u_\xi + (\mu/3) \left(\xi_x u_\xi + \xi_y v_\xi + \xi_z w_\xi\right) \xi_x \\ \mu \left(\xi_x^2 + \xi_y^2 + \xi_z^2\right) v_\xi + (\mu/3) \left(\xi_x u_\xi + \xi_y v_\xi + \xi_z w_\xi\right) \xi_y \\ \mu \left(\xi_x^2 + \xi_y^2 + \xi_z^2\right) w_\xi + (\mu/3) \left(\xi_x u_\xi + \xi_y v_\xi + \xi_z w_\xi\right) \xi_z \\ \left(\xi_x^2 + \xi_y^2 + \xi_z^2\right) \left[\frac{\mu}{2} \left(u^2 + v^2 + w^2\right)_\xi + k T_\xi\right] \\ + \frac{\mu}{3} \left(\xi_x u + \xi_y v + \xi_z w\right) \left(\xi_x u_\xi + \xi_y v_\xi + \xi_z w_\xi\right) \end{array} \right\} \ , \\
\overline{F}_v &= \frac{J^{-1}}{Re} \left\{ \begin{array}{c} 0 \\ \mu \left(\eta_x^2 + \eta_y^2 + \eta_z^2\right) u_\eta + (\mu/3) \left(\eta_x u_\eta + \eta_y v_\eta + \eta_z w_\eta\right) \eta_x \\ \mu \left(\eta_x^2 + \eta_y^2 + \eta_z^2\right) v_\eta + (\mu/3) \left(\eta_x u_\eta + \eta_y v_\eta + \eta_z w_\eta\right) \eta_y \\ \mu \left(\eta_x^2 + \eta_y^2 + \eta_z^2\right) w_\eta + (\mu/3) \left(\eta_x u_\eta + \eta_y v_\eta + \eta_z w_\eta\right) \eta_z \\ \left(\eta_x^2 + \eta_y^2 + \eta_z^2\right) \left[\frac{\mu}{2} \left(u^2 + v^2 + w^2\right)_\eta + k T_\eta\right] \\ + \frac{\mu}{3} \left(\eta_x u + \eta_y v + \eta_z w\right) \left(\eta_x u_\eta + \eta_y v_\eta + \eta_z w_\eta\right) \end{array} \right\} \ , \\
\overline{G}_v &= \frac{J^{-1}}{Re} \left\{ \begin{array}{c} 0 \\ \mu \left(\zeta_x^2 + \zeta_y^2 + \zeta_z^2\right) u_\zeta + (\mu/3) \left(\zeta_x u_\zeta + \zeta_y v_\zeta + \zeta_z w_\zeta\right) \zeta_x \\ \mu \left(\zeta_x^2 + \zeta_y^2 + \zeta_z^2\right) v_\zeta + (\mu/3) \left(\zeta_x u_\zeta + \zeta_y v_\zeta + \zeta_z w_\zeta\right) \zeta_y \\ \mu \left(\zeta_x^2 + \zeta_y^2 + \zeta_z^2\right) w_\zeta + (\mu/3) \left(\zeta_x u_\zeta + \zeta_y v_\zeta + \zeta_z w_\zeta\right) \zeta_z \\ \left(\zeta_x^2 + \zeta_y^2 + \zeta_z^2\right) \left[\frac{\mu}{2} \left(u^2 + v^2 + w^2\right)_\zeta + k T_\zeta\right] \\ + \frac{\mu}{3} \left(\zeta_x u + \zeta_y v + \zeta_z w\right) \left(\zeta_x u_\zeta + \zeta_y v_\zeta + \zeta_z w_\zeta\right) \end{array} \right\} \ . \end{aligned} \tag{4}$$

One should observe that all cross derivative terms have been eliminated in the above expressions of the viscous flux vectors. The computational grids utilised in the simulations do not give support for capturing the neglected viscous terms. Furthermore, for the Reynolds number of interest here, these terms can really be neglected if compared to the ones already considered in this formulation, without limiting the validity of the resulting set of equations. Hence, the equations actually implemented should be regarded as some form of the thin-layer approximation to the Navier-Stokes equations.

The Reynolds number, based on the freestream speed of sound, a_∞, density, ρ_∞, viscosity, μ_∞, and vehicle diameter, d, is given as $Re = \rho_\infty a_\infty d / \mu_\infty$. The Boussinesq hypothesis is used in this work in order to include the turbulent effects in the formulation. Thus, in the viscous terms previously presented, the dynamic viscosity, μ, can be written as $\mu = \mu_\ell + \mu_t$, where μ_ℓ is the laminar viscosity and μ_t is the eddy viscosity, obtained throught the turbulence models chosen.

In the usual CFD nomenclature, adopted in the present work, ρ is the density, u, v and w are the Cartesian velocity components, p is the pressure and e is the total energy per unity of volume. The pressure is obtained from the equation of state for perfect gases, written as

$$p = (\gamma - 1) \left[e - \frac{1}{2} \rho \left(u^2 + v^2 + w^2\right) \right] \ , \tag{5}$$

where γ is the ratio of specifics heats. The contravariant velocity components, U, V and W, were defined as

$$\begin{aligned} U &= \xi_t + \xi_x u + \xi_y v + \xi_z w \ , \\ V &= \eta_t + \eta_x u + \eta_y v + \eta_z w \ , \\ W &= \zeta_t + \zeta_x u + \zeta_y v + \zeta_z w \ . \end{aligned} \tag{6}$$

Throughout this work, the curvilinear coordinate system is defined such that ξ is the rocket longitudinal direction, positive downstream, η is the wall-normal direction, and ζ is the circumferential direction. Expressions for the Jacobian of the transformation, J, and for the various metric terms can be found in Pulliam and Steger, 1980. As already pointed out, one should note that, despite the inclusion of the viscous terms in the ξ and ζ directions, cross derivative terms are not considered in this formulation. Moreover, the meshes used in the simulations do not give support to viscous dissipation in those directions. Therefore, the formulation should be referred as a thin-layer model.

3. Numerical Formulation

The governing equations are discretised in a finite difference context. The spatial discretisation adopted uses a central difference algorithm plus explicitly added artificial dissipation terms in order to control nonlinear instabilities. The equations, fully discretised in space, can be written as

$$\left(\frac{\partial \overline{Q}}{\partial \tau}\right)_{i,j,k} = -\mathrm{RHS}_{i,j,k} \ . \tag{7}$$

The right-hand side operator of Eq. (7) is defined as

$$\begin{aligned} \mathrm{RHS}_{i,j,k} &= \frac{1}{2\,\Delta\xi}\left(\overline{E}_{i+1,j,k} - \overline{E}_{i-1,j,k}\right) + \frac{1}{2\,\Delta\eta}\left(\overline{F}_{i,j+1,k} - \overline{F}_{i,j-1,k}\right) + \frac{1}{2\,\Delta\zeta}\left(\overline{G}_{i,j,k+1} - \overline{G}_{i,j,k-1}\right) \\ &- \frac{1}{\Delta\xi}\left[\left(\overline{E}_{v_{i+1/2,j,k}} - \overline{E}_{v_{i-1/2,j,k}}\right) + J^{-1}_{i+1/2,j,k}\, d_{i+1/2,j,k} - J^{-1}_{i-1/2,j,k}\, d_{i-1/2,j,k}\right] \\ &- \frac{1}{\Delta\eta}\left[\left(\overline{F}_{v_{i,j+1/2,k}} - \overline{F}_{v_{i,j-1/2,k}}\right) + J^{-1}_{i,j+1/2,k}\, d_{i,j+1/2,k} - J^{-1}_{i,j-1/2,k}\, d_{i,j-1/2,k}\right] \\ &- \frac{1}{\Delta\zeta}\left[\left(\overline{G}_{v_{i,j,k+1/2}} - \overline{G}_{v_{i,j,k-1/2}}\right) + J^{-1}_{i,j,k+1/2}\, d_{i,j,k+1/2} - J^{-1}_{i,j,k-1/2}\, d_{i,j,k-1/2}\right] \ , \end{aligned} \tag{8}$$

where $\Delta\xi = \Delta\eta = \Delta\zeta = 1$ for the general curvilinear coordinate case. An anisotropic scalar artificial dissipation method, as described in Turkel and Vatsa, 1994, was used. This scheme is nonlinear and allows a selection between artificial dissipation terms of second and fourth differences, which is very important in capturing shock waves in the flow.

Time march uses an explicit, second order, five-stage Runge-Kutta scheme, derived from the ideas presented in Jameson et al., 1981, which can be written as

$$\begin{aligned} \overline{Q}^{(0)}_{i,j,k} &= \overline{Q}^{n}_{i,j,k} \ , \\ \overline{Q}^{(\ell)}_{i,j,k} &= \overline{Q}^{(0)}_{i,j,k} - \alpha_\ell\, \Delta t_{i,j,k}\, \mathrm{RHS}^{(\ell-1)}_{i,j,k} \ , \qquad \ell = 1, 2, \ldots, 5, \\ \overline{Q}^{n+1}_{i,j,k} &= \overline{Q}^{(5)}_{i,j,k} \ . \end{aligned} \tag{9}$$

Numerical values for the α_ℓ parameters can be found in Jameson and Mavriplis, 1986. In the previous expressions, Δt stands for the time step, and n and $n+1$ refer to the property values at the start and at the end of each time step. Equation (9) also indicates that a local time step option is being used in order to accelerate convergence to steady state calculations.

4. Boundary Conditions and Computational Grids

For the configurations of interest here, the types of boundary conditions that should be considered include upstream (entrance), solid wall, far field boundary, symmetry, upstream centerline and downstream (exit) conditions. For the wall, the velocity vector is set to zero, and a zero-order extrapolation of the pressure and the density is performed. The rocket upstream centerline is a singularity of the coordinate transformation and, hence, an adequate treatment of this boundary must be provided. In the present case, the approach consists in extrapolating the property values from the adjacent longitudinal plane and in averaging the extrapolated values in the azimuthal direction in order to define the updated properties at the upstream centerline. At the exit plane for both configurations, and at the entrance plane for the flat plate, the boundary conditions are implemented through the use of the 1-D characteristic relations for the 3-D Euler equations. The interested

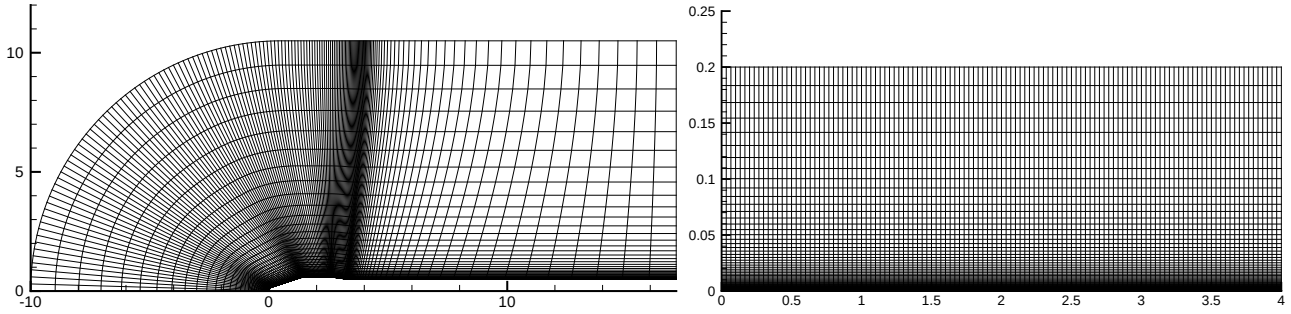

(a) VLS (b) Flat plate

Figure 1: Overall view of a plane from the computational grids used in the simulations performed.

reader is referred to the work of Azevedo et al., 1995, for further details on the use of 1-D characteristic relations for boundary condition implementation. Freestream properties are assumed at the far field boundaries.

In order to reduce computational costs, the grid used in the numerical simulations for the rocket configuration are generated for half a body in the azimuthal direction. This simplification is valid for the cases assessed in this work because low angles of attack are considered. This condition implies a symmetric flow about the pitching plane, as indicated by Ying, 1986. Hence, symmetry is applied in this pitching plane using two auxiliary planes. Those extra elements are added, respectively, before the leeside and after the windside pitching planes. In the case of the flat plate, spanwise symmetry boundary condition is applied to these planes.

Furthermore, in order to correctly simulate the complicated turbulence dynamics that occur inside the boundary layers, a good mesh refinement in these regions is strongly recommended. In a straightforward practical way, the turbulent dimensionless parameter y^+, defined as $y^+ = y\sqrt{\frac{Re}{\nu}\frac{\partial u}{\partial y}}$, where y is the dimensionless distance to the wall of the first mesh point away from it, should be kept around 1. This condition is very important in turbulent simulations in order not to spoil the balance between turbulent production and destruction inside the viscous sublayer. The resulting grid for the VLS main body configuration, to which numerical results are mesh independent, had $156 \times 85 \times 21$ points. For this study, the number of points is the three directions were varied from coarse to refined grids. The numerical solutions were compared to each other until the differences fell below a small value. It was observed that, for very coarse grids in the normal direction, the turbulence model practically spoiled the solution due to the already discussed unbalance of turbulence variables in the boundary layer. For grids with $y^+ < 3$ the numerical solution was grid independent. A view of a longitudinal plane of the VLS grid is shown in Fig. 1. The final mesh for the flat plate configuration had $121 \times 90 \times 10$ points. A view of a longitudinal plane of this grid is shown in Fig. 1. The flat plate length comprises the last 3/4 part of the total computational domain length. For the first 1/4 section, symmetry boundary condition is used.

5. Turbulence Models

As already discussed, turbulence models based on the Boussinesq hypothesis were chosen for this numerical code. Previous work, such as Azevedo and Buonomo, 1999, among others, has shown that advanced turbulence closures are required to correctly address the flow phenomena that may occur about the geometries of interest for the group. Thus, a single- and a two-equation turbulence models, which were originally designed to aerospace applications, were chosen for this work.

The single equation model chosen is the one proposed by Spalart and Allmaras, 1994. This model, rewritten for a compressible flow and considering a general, body-conforming coordinate system, is given in its dimensionless form by

$$\begin{aligned} \frac{\partial \overline{\tilde{\mu}}}{\partial \tau} &+ \frac{\partial\left(\overline{\tilde{\mu}}U\right)}{\partial \xi} + \frac{\partial\left(\overline{\tilde{\mu}}V\right)}{\partial \eta} + \frac{\partial\left(\overline{\tilde{\mu}}W\right)}{\partial \zeta} = J^{-1}\rho c_{b1}\tilde{S}\tilde{\nu} \\ &+ J^{-1}\frac{1}{Re}\frac{1}{\sigma}\left\{\frac{\partial}{\partial x_j}\left[\left(\mu+\tilde{\mu}\right)\frac{\partial \tilde{\nu}}{\partial x_j}\right] + c_{b2}\frac{\partial \tilde{\nu}}{\partial x_k}\frac{\partial \tilde{\nu}}{\partial x_k}\right\} - J^{-1}\frac{1}{Re}\rho c_{w1} f_w \left(\frac{\tilde{\nu}}{d}\right)^2 . \end{aligned} \tag{10}$$

The variable solved by this equation, $\overline{\tilde{\mu}}$, is defined as $\overline{\tilde{\mu}} = J^{-1}\tilde{\mu}$, where $\tilde{\mu} = \rho\tilde{\nu}$. Variable $\tilde{\nu}$ relates to the eddy viscosity by

$$\nu_t = \tilde{\nu} f_{v1} , \qquad f_{v1} = \frac{\chi^3}{\chi^3 + {c_{v1}}^3} , \qquad \chi = \frac{\tilde{\nu}}{\nu} , \tag{11}$$

where ν is the laminar kinematic viscosity, μ is the laminar dynamic viscosity previously defined as μ_ℓ and $x_i = (x, y, z)$ are the cartesian coordinates. The production term, $\tilde{S}$, is given by

$$\tilde{S} = S + \frac{1}{Re}\frac{\tilde{\nu}}{\kappa^2 d^2} f_{v2} \ , \qquad f_{v2} = 1 - \frac{\chi}{1 + \chi f_{v1}} \ , \tag{12}$$

where S is the magnitude of the vorticity vector

$$S = \sqrt{2\Omega_{ij}\Omega_{ij}} \ , \qquad \Omega_{ij} = \frac{1}{2}\left(\frac{\partial u_i}{\partial x_j} - \frac{\partial u_j}{\partial x_i}\right) \ , \tag{13}$$

and $u_i = (u, v, w)$ are the Cartesian components of velocity. Variable d represents the distance to the closest wall. The wall function, f_w, is

$$f_w = g\left[\frac{1 + {c_{w3}}^6}{g^6 + {c_{w3}}^6}\right]^{\frac{1}{6}} \ , \qquad g = r + c_{w2}\left(r^6 - r\right) \ , \qquad r = \frac{1}{Re}\frac{\tilde{\nu}}{\tilde{S}\kappa^2 d^2} \ . \tag{14}$$

Boundary conditions are $\tilde{\nu} = 0$ at the wall and $\tilde{\nu} \leq \frac{\nu}{10}$ at freestream boundaries. A 0-th order extrapolation is chosen for other boundaries. Initial conditions are the same of the freestream values. The model constants are $c_{b1} = 0.1355$, $\sigma = \frac{2}{3}$, $c_{b2} = 0.622$, $\kappa = 0.41$, $c_{w1} = \frac{c_{b1}}{\kappa} + \frac{(1+c_{b2})}{\sigma}$, $c_{w2} = 0.3$, $c_{w3} = 2$ and $c_{v1} = 7.1$.

The two-equation closure chosen is the baseline model (BSL) proposed by Menter, 1993. This model is derived from both the famous $k - \omega$ (Wilcox, 1993) and the standard $k - \epsilon$ models. It solves some reported problems of the $k - \omega$ closure regarding freestream value dependency (Menter, 1994) while keeping the better numerical behaviour of this model at the wall when compared to $k - \epsilon$ closures. The BSL model, rewritten for a compressible flow and considering a general, body-conforming coordinate system, can be given in its dimensionless form as

$$\frac{\partial \overline{k}}{\partial \tau} + \frac{\partial\left(\overline{k}U\right)}{\partial \xi} + \frac{\partial\left(\overline{k}V\right)}{\partial \eta} + \frac{\partial\left(\overline{k}W\right)}{\partial \zeta} = \frac{J^{-1}}{Re}P_k - J^{-1}\beta^*\rho\omega k + \frac{J^{-1}}{Re}\frac{\partial}{\partial x_j}\left[\left(\mu + \mu_t\sigma_k\right)\frac{\partial k}{\partial x_j}\right] \ , \tag{15}$$

$$\begin{aligned}\frac{\partial \overline{\omega}}{\partial \tau} + \frac{\partial\left(\overline{\omega}U\right)}{\partial \xi} + \frac{\partial\left(\overline{\omega}V\right)}{\partial \eta} + \frac{\partial\left(\overline{\omega}W\right)}{\partial \zeta} &= J^{-1}\frac{\gamma_t}{\nu_t}P_k - J^{-1}\beta_1\rho\omega^2 + \frac{J^{-1}}{Re}\frac{\partial}{\partial x_j}\left[\left(\mu + \mu_t\sigma_\omega\right)\frac{\partial \omega}{\partial x_j}\right] \\ &+ J^{-1}2\left(1 - F_1\right)\rho\sigma_{\omega 2}\frac{1}{\omega}\frac{\partial k}{\partial x_j}\frac{\partial \omega}{\partial x_j} \ .\end{aligned} \tag{16}$$

The turbulent variables solved by this set of transport equations are given by

$$\overline{k} = J^{-1}\rho k \ , \qquad \overline{\omega} = J^{-1}\rho\omega \ , \tag{17}$$

where k is the turbulent kinetic energy and ω is the turbulent dissipation. The eddy viscosity is defined by

$$\mu_t = Re\frac{\rho k}{\omega} \ , \tag{18}$$

and the production term is given by

$$P_k = \mu_t\left[\left(\frac{\partial u_i}{\partial x_j} + \frac{\partial u_j}{\partial x_i}\right)\frac{\partial u_i}{\partial x_j} - \frac{2}{3}\left(\frac{\partial u_m}{\partial x_m}\right)^2\right] - \frac{2}{3}Re\,\rho\,k\frac{\partial u_n}{\partial x_n} \ . \tag{19}$$

The following choice of freestream conditions was chosen

$$\omega_\infty = 5\frac{M_\infty}{L} \ , \qquad \nu_{t\infty} = 0.01\nu_\infty \ , \qquad k_\infty = \frac{1}{Re}\nu_{t\infty}\omega_\infty \ , \tag{20}$$

where L is the approximate length of the computational domain. Wall boundary conditions considered were

$$k = 0 \ , \qquad \omega = 60\frac{1}{Re}\frac{\nu}{\beta(\Delta y_1)^2} \ , \tag{21}$$

where Δy_1 is the distance to the wall of the closest point away from it. Zero-th order extrapolation is performed at other boundaries.

The F_1 variable is a blending function that turns on the $k - \omega$ closure near walls and the standard $k - \epsilon$ outside boundary layers. It is given by

$$F_1 = tanh\left(arg_1^4\right) \ , \qquad arg_1 = \min\left[\max\left(\frac{\sqrt{k}}{0.09\omega d}, \frac{500\nu}{Re\omega d^2}\right), \frac{4\rho\sigma_{\omega 2}k}{CD_{k\omega}d^2}\right] \ , \tag{22}$$

where

$$CD_{k\omega} = \max\left(2\rho\sigma_{\omega 2}\frac{1}{\omega}\frac{\partial k}{\partial x_j}\frac{\partial \omega}{\partial x_j}, 10^{-20}\right) \ . \tag{23}$$

Any model constants are generally calculated as

$$\phi = F_1\phi_1 + (1 - F_1)\phi_2 \ , \tag{24}$$

where ϕ_1 represents the set of constants for the $k-\omega$ model and ϕ_2 the set for the standard $k-\epsilon$ model. The following sets were used:

$$\sigma_{k1} = 0.5 \ , \ \sigma_{\omega 1} = 0.5 \ , \ \beta_1 = 0.075 \ , \ \beta^* = 0.09 \ , \ \kappa = 0.41 \ , \ \gamma_{t1} = \frac{\beta_1}{\beta^*} - \frac{\sigma_{\omega 1}\kappa^2}{\sqrt{\beta^*}} \ , \tag{25}$$

$$\sigma_{k2} = 1.0 \ , \ \sigma_{\omega 2} = 0.855 \ , \ \beta_2 = 0.0828 \ , \ \beta^* = 0.09 \ , \ \gamma_{t2} = \frac{\beta_2}{\beta^*} - \frac{\sigma_{\omega 2}\kappa^2}{\sqrt{\beta^*}} \ . \tag{26}$$

Since a measure of the turbulent kinetic energy is used in this model, this should be included in the viscous terms of the Navier-Stokes equations. Therefore, the static pressure is given by

$$p = (\gamma - 1)\left[e - \frac{1}{2}\rho\left(u^2 + v^2 + w^2\right) - \rho k\right] \ , \tag{27}$$

and the new viscous flux arrays are redefined, already considering the thin-layer approximation of the derivatives, as

$$A_{new} = A - \left\{ \begin{array}{c} 0 \\ \frac{2}{3}\overline{k}\psi_x \\ \frac{2}{3}\overline{k}\psi_y \\ \frac{2}{3}\overline{k}\psi_z \\ \frac{2}{3}\overline{k}\left(C - \psi_t\right) - \frac{J^{-1}}{Re}\left(\mu + \mu_t\sigma_{k1}\right)\left(\psi_x^2 + \psi_y^2 + \psi_z^2\right)k_\psi \end{array} \right\} \ , \tag{28}$$

where $A = \overline{E}_v$, $\overline{F}_v$ or $\overline{G}_v$, $\psi = \xi$, η or ζ and $C = U$, V or W, respectively.

The turbulence equations of both models are solved in a decoupled fashion from the Navier-Stokes system. An ADI method, similar to a Beam-Warming scheme (Warming and Beam, 1978), is chosen for the time stepping of the turbulence equations. Artificial viscosity to control non-linear instabilities is added through an upwind discretization of the advective terms of the turbulence equations. This approach is used for both right- and left-hand side operators of the system. The upwind discretization chosen is a flux-vector splitting-type approach similar the Steger-Warming method (Steger and Warming, 1981).

6. Results and Discussions

In this section, the numerical results obtained with the formulation presented here are compared to known data in order to verify the correctness of the implementation and assess the quality of the results that can be obtained with the computational tool under development.

6.1. Flat Plate Results

Figure 2 presents zero pressure gradient flat plate turbulent boundary layer profiles. This flow is an excelent test case for a solver validation since it allows the comparison of the numerical results with an analytical solution. This avoids the uncertainty associated with experimental results, which are another option for validation. One can observe in Fig. 2 the numerical curves obtained with the turbulence closures discussed before, namely, the single-equation Spalart-Allmaras (SA) and the two-equation Menter (BSL) models. The theoretical log-layer profile is also shown in this figure in order to compare with the numerical results. The numerical Reynolds number of the test was $Re = 1$ million. However, the results presented in Fig. 2 are independent of this parameter. It can be clearly seen in this figure that both numerical solutions compare very well with the theoretical solution. This theoretical curve is given by small circles representing the mesh spacing along the normal direction to the wall. One can verify that the first grid point away from the wall has about $y^+ = 0.4$, which is, by far, enough to correctly simulate a turbulent boundary layer with the closures discussed in this work. Small differences can be found between the two models in the intermediate sublayer region. The BSL model estimated a smoother velocity profile than that of the SA closure. However, both estimated very well the viscous and inertial sublayers as well as the external layer. The results presented in Fig. 2 are indicative of the quality of the data that can be obtained with this numerical formulation.

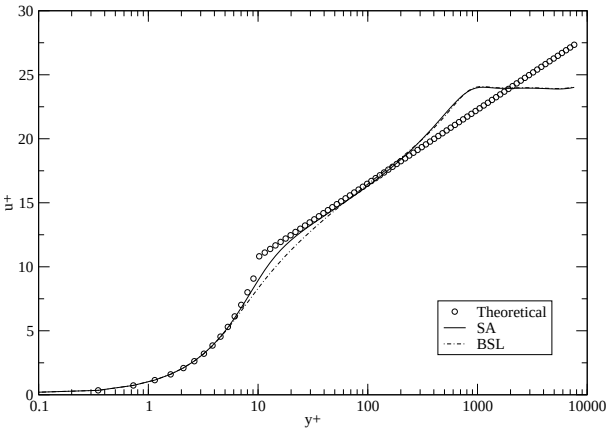

Figure 2: Turbulent boundary layers for a zero pressure gradient flat plate. Numerical Reynolds number is $Re = 1$ million.

6.2. VLS Results

In this section, numerical results for the transonic flow about the VLS second-stage flight configuration, at freestream Mach number $M_\infty = 0.90$ and angle of attack $\alpha = 0$ deg., are presented. The numerical results are compared to available experimental data, obtained through numerous wind tunnel testings, in order to address the correctness of the numerical method implemented. These experimental data were presented in Augusto Neto, 1991, and no information about experimental uncertainty was available in this work. Nevertheless, these are reliable results and they were used for the aerodynamic design of the first VLS.

It should be stated here that the inviscid and the laminar viscous formulation of the computational code presented here were extensively studied in previous work, as can be seen in Bigarelli et al., 2001. In that paper, a large range of flow conditions, such as transonic to supersonic speeds and various angles of attack, was simulated. As a general assessment, good results within engineering error margins could be obtained. It is important to note, however, that these simulations were not correct in the sense that high Reynolds number were considered, for which the real flow is actually turbulent. Nevertheless, these computations were done in order to validate the numerical tool. In the present work, inviscid and laminar simulations are also performed for such high Reynolds numbers. Thus, the reader must keep in mind that these are just intermediary solutions towards a turbulent flow simulation capability, which is the correct flow representation.

The turbulent simulation results presented here were obtained with the newly implemented turbulence modelling capability added to the code. Furthermore, the transonic flight condition was chosen due to its physical complexity which results in a more difficult simulation case. In this flight condition, a strong shock wave builds over the vehicle payload fairing and other flow regions are still transonic, as will be seen in the forthcoming results. Besides the known mathematical complexity that this situation may impair to the simulation, this strong shock wave may interfere with the boundary layer in that region, interacting with it in a very complicated fashion. Previous axisymmetric results (Azevedo and Buonomo, 1999; Strauss, 2001) showed that turbulence modelling is required to correctly capture the flow configuration in this region. As will be seen, the flow complexity is large enough to prevent the laminar formulation from converging to a steady-state solution.

Figure 3 presents experimental and numerical Mach number contours over the VLS central body at freestream Mach number $M_\infty = 0.90$ and angle of attack $\alpha = 0$ deg. Various approximations to the Navier-Stokes equations were used to simulate the transonic flow over the VLS second-stage flight configuration, including an inviscid, a laminar viscous ($Re = 30$ million) and two turbulent ($Re = 30$ million) closure approaches. For the latter computations, the two turbulence models described in the last section were used. A less refined mesh than presented in Fig. 1 was used in the inviscid simulation. One can see in Fig. 3 that the inviscid and the turbulent results are qualitatively alike the experimental data ($Re = 25$ million). The presence of a strong shock wave that builds over the vehicle payload fairing region is clear. For the inviscid case, however, shocks and expansions are obviously stronger since a boundary layer is not present in the solution. One can also verify that the laminar result is much different from the experimental one. The laminar flow separates at the first expansion corner due to the weakness of the laminar boundary layer at such a high Reynolds number. The separated flow, in this simulation, had an unsteady behaviour and kept the computations from converging to a steady-state solution. This statement is corroborated by the oscillating residue history curve that can be seen in Fig. 4. This figure presents the residue history for the four methods considered in Fig. 3. The maximum density residue field value was used as the measure of convergence of the method. The inviscid and the turbulent simulations converged to a steady-state solution. Furthermore, the non-symmetrical results observed in Fig. 3 are also indicative of a

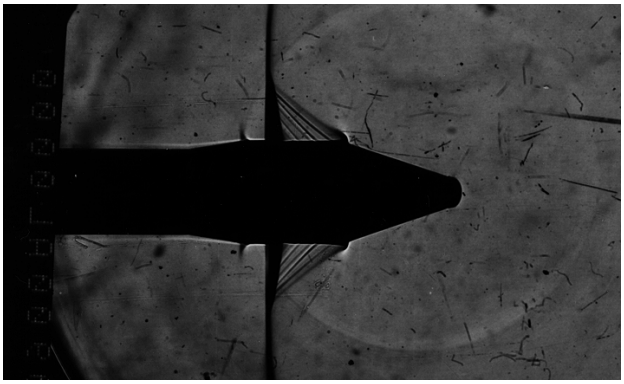

(a) Experimental (Schlieren).

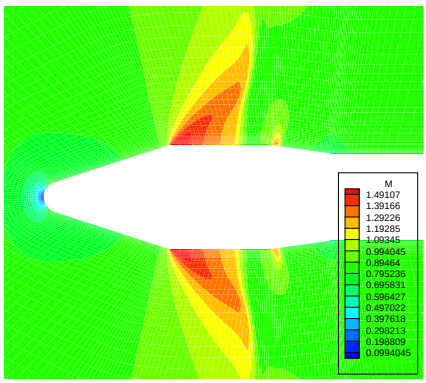

(b) Inviscid.

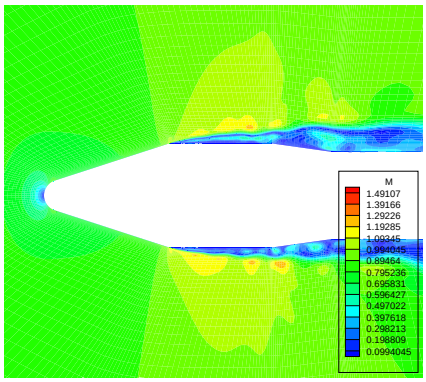

(c) Laminar.

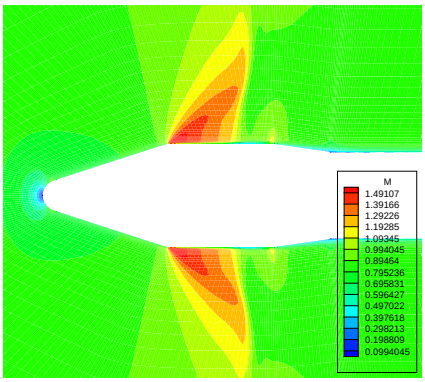

(d) Turbulent (SA).

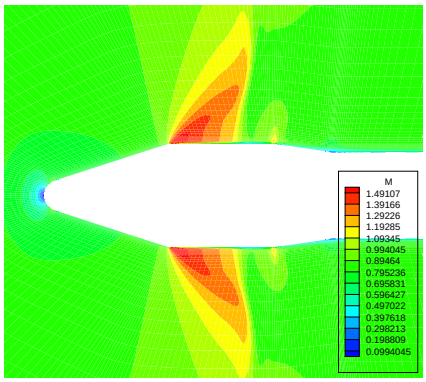

(e) Turbulent (BSL).

Figure 3: Experimental and numerical Mach number contours over the VLS second stage configuration at $M_\infty = 0.90$ and $\alpha = 0$ deg. Numerical Reynolds number was $Re = 30$ million and the experimental one was $Re = 25$ million.

transient numerical solution. One should observe, however, that since a variable time step option is used in the present simulations, such an unsteady solution does not represent the actual physical transient behaviour.

Figure 5 presents pressure contours for the VLS main body at the same flight condition of Fig. 3. This result was obtained with the laminar formulation. In this figure, streamlines are also included to indicate the vortex structures that build due to the flow separation. These seem to be convected by the mean flow in a similar fashion as a von Kármán vortex street. This is corroborated by the fact that the simulation was characterised by a transient solution, as seen before. Furthermore, the results presented in Fig. 6 relate to these statements. This figure presents Cp distributions along the vehicle wall for both lee- and windside pitching planes. It should be noted the oscillatory and non-symmetrical behaviour of the curves. The results presented so far corroborate the statement that a good turbulence modelling is necessary to correctly simulated such a complicated flow.

Figure 7 presents the numerical and experimental Cp wall distributions for the geometry described before at freestream Mach number $M_\infty = 0.90$ and angle of attack $\alpha = 0$ deg. This figure shows numerical results obtained with the inviscid and the two turbulent approximations discussed before. The laminar results were not included for obvious reasons. It can be seen in Fig. 7 that the inviscid simulation presents overshoots at high gradient regions, such as the shock wave and sharp corners along the geometry. This behaviour is well known for this formulation. It can also be seen that the turbulent simulations followed much better the experimental pressure distribution, if compared to the inviscid computations. Both turbulence models performed in a very similar way in this simulation, which is indicative of the quality of the numerical solution that can be expected with the newly implemented turbulence modelling capability. However, a small difference between the numerical solutions and the experimental data can be seen at the shock wave position over the payload fairing region. The turbulent solutions estimated the shock position further downstream than shown in the experimental data. Some aspects may explain this difference observed. The first one regards the difference between the numerical and the experimental Reynolds number considered. In such a complicated case as this transonic flow, this

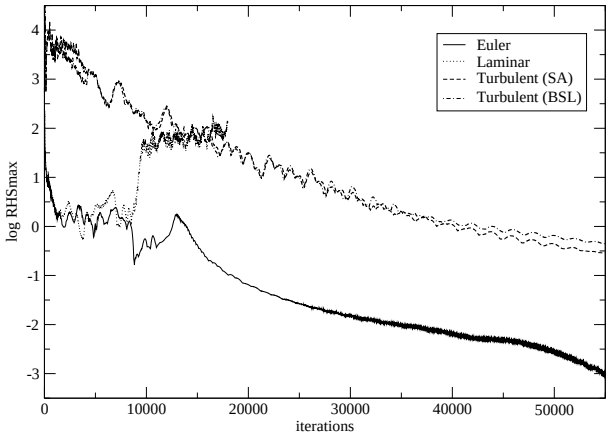

Figure 4: Residue histories obtained with different approximations to the Navier-Stokes equations.

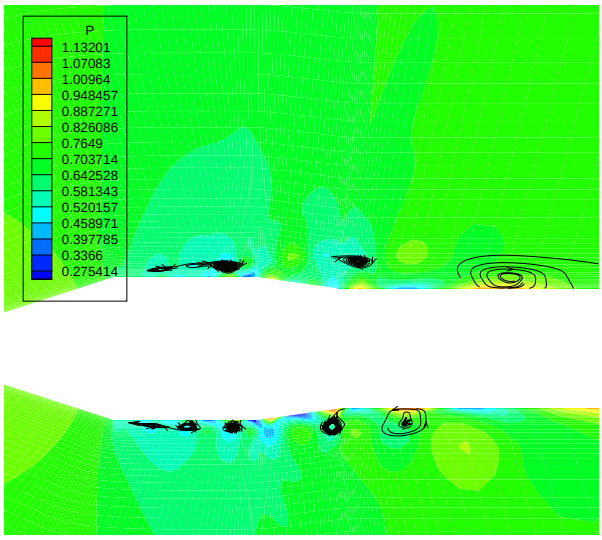

Figure 5: Pressure contours and streamlines over the VLS central body at $M_\infty = 0.90$ and $\alpha = 0$ deg. Numerical Reynolds number was $Re = 30$ million and experimental one was $Re = 25$ million.

can be extremely important to the flow configuration since the shock wave position is fully determined by the formulation itself and, therefore, is not attached to any geometric discontinuity. Another aspect is related to the mesh refinement along the longitudinal direction. A detail of the mesh with the pressure contours in this region, obtained with the simulation with the Spalart-Allmaras model, can be seen in Fig. 8. One can verify in this figure that the mesh may not be refined enough in the longitudinal direction in order to correctly capture the purely viscous phenomena that occur when the shock wave interacts with the boundary layer. Finally, the experimental model used in the wind tunnel tests was tested with the four boosters attached to main body. This fact may have an influence in the shock wave position and the flow configuration since, in subsonic flight conditions, what happens downstream can influence the flow upstream. As already stated, the computational model simulated considered only the vehicle main body configuration. Hence, the slight differences observed in Fig. 7 between numerical and experimental results over the vehicle payload fairing may be explained by the various reason presented. One should further observe that in the afterbody cylindrical section, all numerical results tend to return to the freestream pressure values, i.e., $Cp = 0$. This is not true for the experimental data, which present small, but higher Cp values in this region. This is clearly the influence of the strap-on boosters which are not included in the numerical simulations.

The aspects discussed above will be addressed in future work, but the results presented so far are representative of the behaviour and the quality of the turbulent solutions that could be obtained with the present formulation. The last aspect, specially, that concerns the influence of the boosters can be addressed only with a multiblock capability in order to include these geometries in the computational model. This certainly will be a future step for the development of this numerical tool. Preliminary results with a laminar viscous formulation and a multiblock capability were already obtained, as can be seen in Basso et al., 2000.

Another important aspect that should be emphasized which regards the turbulence modelling is the increase

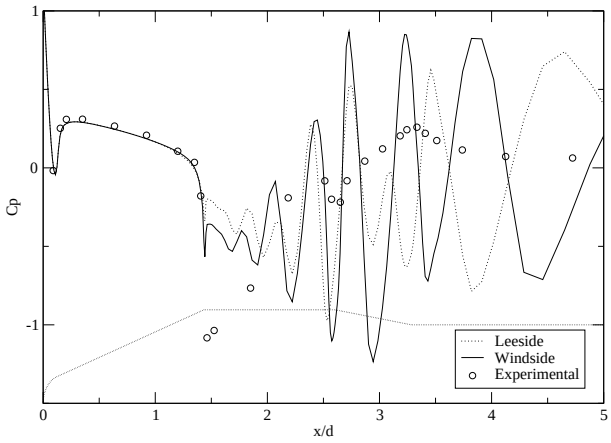

Figure 6: Experimental and numerical Cp distributions over the VLS second stage configuration at $M_\infty = 0.90$ and $\alpha = 0$ deg. obtained with a laminar formulation. The numerical Reynolds number was $Re = 30$ million and the experimental one was $Re = 25$ million.

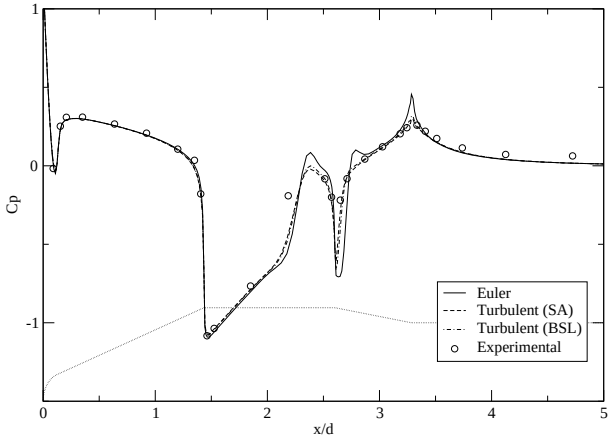

Figure 7: Experimental and numerical Cp distributions over the VLS second stage configuration at $M_\infty = 0.90$ and $\alpha = 0$ deg. obtained with various formulations. The numerical Reynolds number was $Re = 30$ million and the experimental one was $Re = 25$ million.

in the computational resources necessary to address the new equations added to the formulation. A simulation of a laminar flow costs 25% more then an inviscid one, while the same simulation with a single- and a two-equation turbulence modelling costs, respectively, 45% and 50% more then the laminar computations. Added to this is the fact that, as already stated, a turbulent simulation requires more refined and/or stretched grid in order to satisfy the $y^+ = 1$ condition for the first grid point away from the wall. This increases the stiffness of the problem rendering lower convergence rates to the code. This can be observed in the results of Fig. 4. One should note in this figure that the inviscid simulation, with a less refined and stretched grid, converges much faster then the turbulent cases. Finally, one can observe in Fig. 9 the residue histories of the turbulence model equations. This figure presents the maximum residue field value of the turbulent variable been solved. In the case of the SA model, the eddy viscosity variable, $\overline{\tilde{\mu}}$, was used, while, for the BSL model, the turbulent kinetic energy variable, $\overline{k}$, was chosen. It can be seen in Fig. 9 that the turbulent equations converge when the governing equations converge to a steady state solution. This is a good indication that, for typical CFL numbers that can be used with the explicit numerical method presented here, the ADI time marching procedure of the turbulence equations, together with the upwind discretization of the advective terms of this system, are enough to control nonlinear instabilities of these equations. In other words, the turbulence equations do not spoil the convergence of the governing equations, which results in a more robust numerical tool for the applications of interest.

7. Concluding Remarks

This work presents the assessment of the newly implemented turbulent 3-D flow solver capability at IAE. This numerical tool is aimed at solving three-dimensional flows over complex aerospace configurations at angle of attack to determine important aerodynamic loads required at the design stage. Previous results showed the need for incorporating robust turbulent closures to the computational code in order to correctly address the

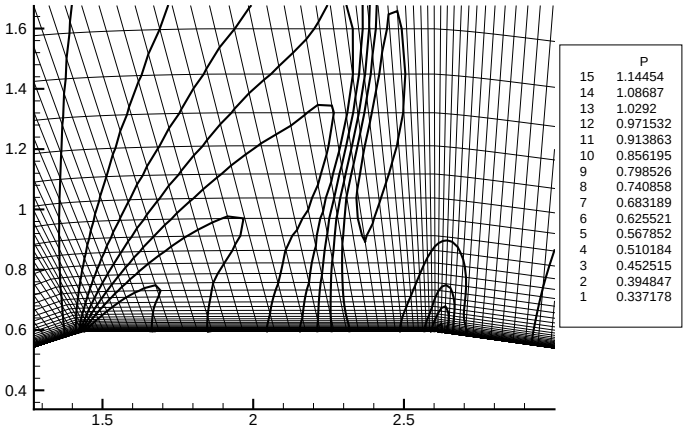

Figure 8: Detail of the mesh in the region where the shock wave interatcs with the boundary layer.

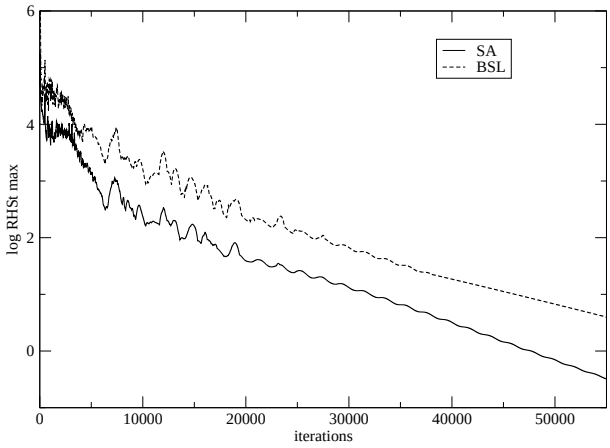

Figure 9: Residue histories for the turbulent equations of the SA and the BSL turbulent models.

transonic and supersonic flow about such complicated geometries. A computational code which solves the compressible Reynolds-averaged Navier-Stokes equations for general, body-conforming, curvilinear coordinates was used. The Spalart-Allmaras single-equation model and Menter's baseline two-equation turbulence closure were implemented into the code in order to include the turbulent influence into the governing equations. The numerical code was used to simulate the subsonic flow about a flat plate and transonic flows about the VLS central body configuration at freestream Mach number of 0.90 and zero angle of attack.

A previous verification analyses involved the comparison of the zero pressure gradient flat plate turbulent boundary layers with the theoretical log-layer law. Very good agreement between the numerical and the theoretical results was obtained. The numerical results for the simulation of the VLS at a transonic Mach number were, then, compared to experimental data in order to further assess the quality of the computational tool. In general, good results were obtained, which showed the capability of this code to adequately address the flows of interest at IAE. An analysis of the computational resources necessary to simulate the turbulent flow showed that one turbulent iteration costs about twice that of an inviscid step for the problem under study. Furthermore, the condition of satisfying $y^+ = 1$ for the first point away from the wall yields more stretched and refined computational meshes. This results in much slower convergence rates. The CFD group at IAE is already working to implement a multigrid method into the code to accelerate convergence to steady-state solutions.

Finally, it can be stated that much more results would be necessary to completely validate this solver. However, this work is an account of the evolutionary process towards the complete flow simulation capability desired. The results presented here are a good indication of the level of accuracy that can be attained with the computational tool even at the present stage of development.

8. Acknowledgements

The present work was partially supported by Conselho Nacional de Desenvolvimento Científico e Tecnológico, CNPq, under the Integrated Project Research Grant No. 522.413/ 96-0. The first author is indebted to Fundação de Amparo à Pesquisa do Estado de São Paulo, FAPESP, which provides him a graduate scholarship. The

authors also acknowledge CESUP, at Universidade Federal do Rio Grande do Sul, for providing the necessary computational resources to address the turbulent simulations presented in this work.

9. Bibliography

Augusto Neto, A., 1991, VLS/PT-01 – Distribution of Normal and Lateral Force Coefficients for the Complete Vehicle Configuration, Technical Report No. 590-0000/B5411, Instituto de Aeronáutica e Espaço, CTA, São José dos Campos, SP, Brazil.

Azevedo, J. L. F. and Buonomo, C. A., 1999, Axisymmetric Turbulent Simulations of Launch Vehicle Forebody Flows, "30th AIAA Fluid Dynamics Conference and Exhibit", AIAA Paper No. 99-3528.

Azevedo, J. L. F., Fico Jr., N. G. C. R., and Ortega, M. A., 1995, Two-Dimensional and Axisymmetric Nozzle Flow Computations Using the Euler Equations, "Journal of the Brazilian Society of Mechanical Sciences", Vol. 17, No. 2, pp. 147–170.

Azevedo, J. L. F., Moraes, Jr., P., Maliska, C. R., Marchi, C. H., and Silva, A. F. C., 1996, Code Validation for High-Speed Flow Simulation over Satellite Launch Vehicle, "Journal of Spacecraft and Rockets", Vol. 33, No. 1, pp. 15–21.

Azevedo, J. L. F., Zdravistch, F., and Silva, A. F. C., 1991, Implementation and Validation of Euler Solvers for Launch Vehicle Flows, "Proceedings of the Fourth International Symposium on Computational Fluid Dynamics", pp. 42–47, Davis, CA, USA.

Basso, E., Antunes, A. P., and Azevedo, J. L. F., 2000, Three Dimensional Flow Simulations Over a Complete Satellite Launcher with a Cluster Configuration, "Proceedings of the 18th AIAA Applied Aerodynamics Conference and Exhibit", AIAA Paper No. 2000-4514, pp. 805–813, Denver, CO, USA.

Bigarelli, E. D. V., Cruz, L. R. S., Azevedo, J. L. F., and Mello, O. A. F., 2001, Normal Force Calculations for a Typical Launch Vehicle Configuration, "Proceedings of the XXII Iberian Latin American Congress on Computational Methods in Engineering – XXII CILAMCE", Campinas, SP, Brazil.

Bigarelli, E. D. V., Mello, O. A. F., and Azevedo, J. L. F., 1999, Three Dimensional Flow Simulations for Typical Launch Vehicles at Angle of Attack, "Proceedings of the 15th Brazilian Congress of Mechanical Engineering – COBEM 99", Article AAAEHA.

Jameson, A. and Mavriplis, D., 1986, Finite Volume Solution of the Two-Dimensional Euler Equations on a Regular Triangular Mesh, "AIAA Journal", Vol. 24, No. 4, pp. 611–618.

Jameson, A., Schmidt, W., and Turkel, E., 1981, Numerical Solution of the Euler Equations by Finite Volume Methods Using Runge-Kutta Time-Stepping Schemes, "Proceddings of the AIAA 14th Fluid and Plasma Dynamics Conference", AIAA Paper 81-1259, Palo Alto, CA, USA.

Menter, F. R., 1993, Zonal Two Equation $k-\omega$ Turbulence Models for Aerodynamic Flows, "AIAA 24th Fluid Conference", pp. 1–20, Orlando, Florida, USA.

Menter, F. R., 1994, Two-Equation Eddy-Viscosity Turbulence Models for Engineering Applications, "AIAA Journal", Vol. 32, No. 8, pp. 1598–1605.

Pulliam, T. H. and Steger, J. L., 1980, Implicit Finite-Difference Simulations of Three-Dimensional Compressible Flow, "AIAA Journal", Vol. 18, No. 2, pp. 159–167.

Spalart, P. R. and Allmaras, S. R., 1994, A One-Equation Turbulence Model for Aerodynamic Flow, "La Recherche Aeropastiale", Vol. 1, pp. 5–21.

Steger, J. L. and Warming, R. F., 1981, Flux Vector Splitting of the Inviscid Gasdynamic Equations with Application to Finite-Difference Methods, "Journal of Computational Physics", Vol. 4, No. 2, pp. 263–293.

Strauss, D., 2001, An Unstructured Grid Approach to the Solution of Axisymmetric Launch Vehicle Flows, Master's thesis, Instituto Tecnológico de Aeronáutica, São José dos Campos, SP, Brazil.

Turkel, E. and Vatsa, V. N., 1994, Effect of Artificial Viscosity on Three-Dimensional Flow Solutions, "AIAA Journal", Vol. 32, No. 1, pp. 39–45.

Warming, R. F. and Beam, R. M., 1978, On the Construction and Application of Implicit Factored Schemes for Conservation Laws, "SIAM-AMS Proceedings", Vol. 11, pp. 85–129.

Wilcox, D. C., 1993, Comparison of Two-Equation Turbulence Models for Boundary Layers with Pressure Gradient, "AIAA Journal", Vol. 31, No. 8, pp. 1414–1421.

Ying, S. X., 1986, Three-Dimensional Implicit Approximately Factored Schemes for the Equations of Gasdynamics, SUDAAR 557, Dept. of Aeronautics and Astronautics, Stanford University, Stanford, CA, USA.

Zdravistch, F. and Azevedo, J. L. F., 1990, Numerical Simulation of High Speed Flows over Complex Satellite Launchers, "Proceedings of the 3rd Brazilian Thermal Sciences Meeting – ENCIT 90", pp. 233–238, Itapema, SC, Brazil.